The Three Hundred: M_{sub}–V_{circ} relation

Atulit Srivastava [1,2]★ Weiguang Cui [1,2,3]★† Massimo Meneghetti [4,5] Romeel Dave [3,5]
Alexander Knebe [1,2,6] Antonio Ragagnin [7,8,9] Carlo Giocoli [4,5] Francesco Calura [4]
Giulia Despali [7,10] Lauro Moscardini [4,5,7] and Gustavo Yepes [1,2]

[1]*Departamento de Física Teórica, M-8, Universidad Autónoma de Madrid, Cantoblanco E-28049, Madrid, Spain*
[2]*Centro de Investigación Avanzada en Física Fundamental (CIAFF), Universidad Autónoma de Madrid, Cantoblanco, E-28049 Madrid, Spain*
[3]*Institute for Astronomy, University of Edinburgh, Royal Observatory, Edinburgh EH9 3HJ, UK*
[4]*INAF-Osservatorio di Astrofisica e Scienza dello Spazio di Bologna, Via Piero Gobetti 93/3, I-40129 Bologna, Italy*
[5]*INFN-Sezione di Bologna, Viale Berti Pichat 6/2, I-40127, Bologna, Italy*
[6]*International Centre for Radio Astronomy Research, University of Western Australia, 35 Stirling Highway, Crawley, Western Australia 6009, Australia*
[7]*Dipartimento di Fisica e Astronomia 'Augusto Righi', Alma Mater Studiorum Università di Bologna, Via Gobetti 93/2, I-40129 Bologna, Italy*
[8]*INAF-Osservatorio Astronomico di Trieste, Via G. B. Tiepolo 11, I-34143 Trieste, Italy*
[9]*IFPU – Institute for Fundamental Physics of the Universe, Via Beirut 2, I-34014 Trieste, Italy*
[10]*Institut für Theoretische Astrophysik, Zentrum für Astronomie, Heidelberg Universität, Albert-Ueberle-Str. 2, D-69120 Heidelberg, Germany*

ABSTRACT

In this study, we investigate a recent finding based on strong lensing observations, which suggests that the sub-haloes observed in clusters exhibit greater compactness compared to those predicted by ΛCDM simulations. To address this discrepancy, we compare the cumulative sub-halo mass function and the M_{sub}–V_{circ} relation between observed clusters and 324 simulated clusters from THE THREE HUNDRED project, focusing on the hydrodynamic resimulations using GADGET-X and GIZMO-SIMBA baryonic models. The cumulative sub-halo mass function of GIZMO-SIMBA simulated clusters aligns with observations, while GADGET-X simulations exhibit discrepancies in the lower sub-halo mass range, possibly due to its strong supernova feedback. Both GADGET-X and GIZMO-SIMBA simulations demonstrate a redshift evolution of the sub-halo mass function and the V_{circ} function, with slightly fewer sub-haloes observed at lower redshifts. Neither the GADGET-X nor GIZMO-SIMBA (albeit a little closer) simulated clusters' predictions for the M_{sub}–V_{circ} relation align with the observational result. Further investigations on the correlation between sub-halo/halo properties and the discrepancy in the M_{sub}–V_{circ} relation reveal that the sub-halo's half mass radius and galaxy stellar age, the baryon fraction, and sub-halo distance from the cluster's centre, as well as the halo relaxation state, play important roles on reproducing this relation. Nonetheless, challenges persist in accurately reproducing the observed M_{sub}–V_{circ} relationship within our current hydrodynamic cluster simulation that adheres to the standard ΛCDM cosmology. These challenges may stem from shortcomings in our baryon modelling, numerical intricacies within the simulation, or even potential limitations of the ΛCDM framework.

Key words: gravitational lensing: strong – galaxies: clusters: general – dark matter.

1 INTRODUCTION

Cold dark matter (CDM) plays an essential role in the formation and evolution of galaxies and galaxy clusters. It can be detected solely through its gravitational effects, such as the bending of light from background galaxies. Galaxy clusters are gravitationally bounded systems with a mass around 10^{14}–10^{15} solar masses, and dark matter constitutes approximately 80 per cent of their mass. Gravity drives the process of structure formation, with haloes assembling hierarchically over time. Galaxy cluster haloes, in particular, are among the structures that form late (White & Frenk [1991]; Tormen [1998]; Giocoli et al. [2007]). Within galaxy clusters, hundreds to thousands of sub-haloes reside in local potential minima (Springel et al. [2001]; Giocoli et al. [2010]). These inner structures are known as sub-haloes. Investigating and understanding these sub-haloes will help us comprehend galaxy cluster formation in detail.

The paper by Meneghetti et al. ([2020]) (hereafter M20) studied the gravitational lensing properties of both cluster haloes and sub-haloes from the Cluster Lensing and Supernova Survey with Hubble (CLASH) (Postman et al. [2012]) and Hubble Frontier Fields (Lotz et al. [2017]) data sets. The study compared these observations with hydrodynamically simulated galaxy clusters. In their study, M20 discovered that the Galaxy-Galaxy Strong Lensing (GGSL) probability from simulation, reconstructed means of the lensing tool of Bergamini et al. ([2019]), is significantly lower compared

★ E-mail: atulit.srivastav@estudiante.uam.es (AS); weiguang.cui@uam.es (WC)
† Talento-CM fellow

to the observed clusters. This finding indicates that the observed clusters have a much higher GGSL probability than those from hydrodynamic simulations under the ΛCDM cosmology. To support their argument, M20 used the maximum circular velocities, V_{circ}.[1], of sub-haloes within galaxy clusters as a metric to assess the degree of compactness, as it directly reflects the sub-halo potential for producing the strong lensing events. This V_{circ} is associated with the 1D-velocity dispersion σ_o by $V_{circ} = \sqrt{2}\sigma_o$, and is one of the parameters in the lens modelling analysis of M20. They observed that the sub-haloes in observed clusters have higher V_{circ} values when compared to sub-halo samples from mass-matched clusters in the cosmological hydrodynamic simulations by Planelles et al. (2014). These findings suggest that galaxies in observed clusters are more efficient at lensing background sources and potentially more concentrated. The discrepancy between simulation and observation results may arise from limitations in the simulation's resolution/baryon models or the presence of systematics. It has been suggested that the simulation output is sensitive to mass resolution and tidal disruption (van den Bosch et al. 2018; Green, van den Bosch & Jiang 2021), which could potentially affect the properties of the sub-haloes. However, Meneghetti et al. (2022) (see also Ragagnin et al. 2022) found that the resolution does not affect the GGSL probability, which, however, seems sensitive to the galaxy formation model implemented in the simulations. Nevertheless, reproducing galaxies' stellar mass function and internal structure simultaneously remains challenging. Another potential explanation is that this issue arises from an inaccurate understanding of the nature of dark matter within the ΛCDM paradigm, which may necessitate the exploration of alternative models such as self-interacting dark matter (SIDM) models (Yang & Yu 2021; Bhattacharyya et al. 2022) and cold and sterile neutrino (SN) dark matter models (Despali et al. 2020).

Using the simulated galaxy clusters from the Hydrangea/C-EAGLE cosmological hydrodynamic simulations, Bahé (2021) conducted a similar comparison to the observed clusters, as in M20. Only one simulated cluster from Hydrangea at redshift $z = 0.4$ matches closely with the mass range of the observed sample presented in M20, with the mass of M_{200c}[2] $> 7.37 \times 10^{14} M_\odot$ They claimed that sub-haloes in this highly resolved simulation align well with the observations (see also another study by Robertson 2021 for resolution impact on the lensing signal in simulations). In particular, Bahé (2021) argued that V_{circ} in Hydrangea is consistent with the observation trend. This increase in the offset of the maximum circular velocity was attributed to the high baryon fractions in the simulations. Bahé (2021) further revealed that sub-haloes with a higher fraction of baryonic matter exhibited higher V_{circ}, implying that dense stellar cores capable of sustaining tidal stripping play a major role in explaining the observed high lensing signals (Armitage et al. 2019, also see Bahé et al. 2019; Joshi et al. 2019). Additionally, Bahé (2021) also checked the result from the Illustris-TNG300 simulation (Pillepich et al. (2018); Springel et al. (2018); Nelson et al. (2019)), and argued that both Illustris-TNG300 and Hydrangea simulations predicted high V_{circ} values for massive sub-haloes located in the vicinity of the cluster centre. Thus, Bahé (2021) concluded that there is no evidence of a significant disagreement between the observed sub-halo concentrations and predictions from the CDM model.

On the contrary, Ragagnin et al. (2022) examined the effects of various numerical setups, such as resolution, softening length, and the AGN feedback scheme, on the interior structure of cluster sub-haloes using six simulated zoomed-in regions of Dianoga. They found contrasting results compared to Bahé (2021). Their findings suggested that, irrespective of the numerical configurations employed, the sub-haloes of simulated clusters were unable to reproduce the observed M_{sub}–V_{circ} (M_{sub}, sub-halo mass) relation from Bergamini et al. (2019). This failure to reproduce the scaling relation was particularly pronounced for sub-halo masses $M_{sub} < 1.47 \times 10^{11} M_\odot$, which corresponds to the mass range of interest for GGSL events. It is worth noting that the results in Bahé (2021) also exhibit a clear offset from the observational result in the M_{sub}–V_{circ} relation at sub-halo mass $M_{sub} \lesssim 10^{11} M_\odot$ (see their Figs 3 and 4). The simulated sub-halo's V_{circ} are approximately 30 per cent smaller compared to the observed scaling relation presented by Bergamini et al. (2019). The scaling relationship between M_{sub} (mass of sub-haloes) and V_{circ}, as derived from simulations, shows good agreement with observations in the high-mass range ($M_{sub} > 5.90 \times 10^{11} M_\odot$). However, concerns have been raised by Ragagnin et al. (2022) regarding the simulations' tendency to produce high-stellar masses for sub-haloes within this mass range. This discrepancy in stellar mass could potentially be a key factor contributing to the observed agreement in the M_{sub}–V_{circ} relation for the high-mass range, and may also be associated with the Hydrangea simulations examined by Bahé (2021). As such, the simulations can reproduce the correct scaling relationship between M_{sub} and V_{circ} by adjusting the AGN feedback strength, the resulting galaxies exhibit unrealistic properties, such as having larger stellar masses compared to observed galaxies. As demonstrated by Ragone-Figueroa et al. (2018), both Hydrangea and IllustrisTNG simulations show excessively large stellar masses in the brightest cluster galaxies. Feedback from supernovae (SNe) exerts a more pronounced influence on galaxies with lower masses. In simulations where SN feedback is weak or absent, low-mass galaxies may not undergo the typical regulation of star formation, resulting in the development of a dense stellar core. This increased density could, in turn, enhance their effectiveness as gravitational lenses. However, we would like to further note that resolution and cluster environment may also have a strong impact on simulation results (for example van den Bosch et al. 2018), which require further detailed studies. In general, the strength of SN and AGN feedback in the simulations is adjusted based on the total galaxy stellar mass function for these cosmological simulations. Meanwhile, the satellite's stellar mass function in THE THREE HUNDRED is utilized for calibrating the GIZMO-SIMBA model (Cui et al. 2022). Consequently, weak or absent feedback may yield results that align with the observed M_{sub}–V_{circ} relation, but it may not necessarily agree with the satellite stellar mass function. Therefore, it is important to emphasize that both Meneghetti et al. (2022) and Ragagnin et al. (2022) clearly stated that their simulations are unable to simultaneously reconcile with the observed M_{sub}–V_{circ} relationship and the satellite stellar mass function in the low sub-halo mass regime.

We would like to point out that all these previous studies are limited by the number of cluster samples, which cannot draw statistically solid conclusions and lack correlation studies. In a recent letter, Meneghetti et al. (2023), performed a ray-tracing analysis of 324 galaxy clusters from the THE THREE HUNDRED[3] and found that the GIZMO-SIMBA version run developed denser stellar cores and boosted the GGSL probability by a factor of ~3 than its GADGET-

---

[1]We will use V_{circ} to denote the maximum circular velocities throughout this paper.

[2]M_{200c} represents the mass within a radius denoted as R_{200c}, measured from the centre of a galaxy cluster's potential, where this radius signifies the region with an average density that is 200 times the critical density of the universe.

[3]https://www.the300-project.org

X counterparts. In this companion paper, we also use the same galaxy clusters from the THE THREE HUNDRED project, as detailed in Cui et al. (2018, 2022), to compare with the observed M_{sub}–V_{circ} relation reported in M20. Although our simulated clusters have a slightly lower mass resolution than Planelles et al. (2014) and about 100 times lower than the Hydrangea simulated clusters, they have a significant advantage in terms of a large sample size, a relatively wide extensive mass range and, importantly, two different baryon models. Our sample includes approximately 15 times more simulated clusters than the Dianoga simulation used in Ragagnin et al. (2022). These advantages allow us to statistically investigate and understand the discrepancy.

The paper is organized as follows. In Section 2, we introduce the THE THREE HUNDRED galaxy cluster simulation with the Amiga Halo Finder (AHF) halo catalogue, which we used to identify host-haloes and their corresponding sub-haloes. We will also explain our methodology for selecting the samples of host haloes and their sub-haloes. In Section 3, we compare the sub-halo mass distribution of M20 to three reference clusters with the predictions from the simulation and examine how it evolves with redshift. In Section 4, we present the cumulative sub-halo's V_{circ} function for the simulations. In Section 5, we compare the observed M_{sub} and V_{circ} relation reported in Bergamini et al. (2019) with the one generated from the data set of simulated clusters in the THE THREE HUNDRED project. We also examine the influence of sub-halo and host-halo properties on the M_{sub}–V_{circ} relationship. Finally, in Section 6 we summarize our results.

2 SIMULATIONS

The THE THREE HUNDRED project, introduced in Cui et al. (2018), consists of an ensemble of 324 galaxy clusters that were modelled based on the extraction of a mass-complete sample with the largest virial halo mass $M_{vir} \gtrsim 1.18 \times 10^{15}$ M$_\odot$ at $z = 0$ from the Dark Matter-only Multidark simulation (MDPL2, Klypin et al. 2016). The MDPL2 simulation employs periodic boundary conditions with a cubic side of 1 Gpc h^{-1} and contains 3840^3 dark matter particles, with a mass of 2.21×10^9 M$_\odot$. This dark matter-only simulation adopts cosmological parameters ($\Omega_M = 0.307$, $\Omega_B = 0.048$, $\Omega_\Lambda = 0.693$, $h = 0.678$, $\sigma_8 = 0.823$, $n_s = 0.96$) based on the Planck observations from Planck Collaboration et al. (2016). Each selected cluster is placed at the centre of the resimulated box inside a high-resolution spherical region with a radius of 22.13 Mpc. The regions are filled with gas and dark matter particles (with $m_{DM} = 1.87 \times 10^9$ M$_\odot$ and $m_{gas} = 3.48 \times 10^8$ M$_\odot$) based on the original dark matter distribution, following the cosmological baryon fraction $\Omega_B = 0.048$. Beyond the 15 h^{-1}Mpc range, the outer region is populated with low-resolution mass particles to simulate any large scale tidal effects similar in a computationally efficient way compared to the original MDPL2 simulation. Subsequently, the 324 selected regions undergo resimulation using different baryonic models and codes, namely GADGET-X (Rasia et al. 2015) and GIZMO-SIMBA (Davé et al. 2019; Cui et al. 2022). For each cluster simulated in the THE THREE HUNDRED project using GADGET-X and GIZMO-SIMBA, we have 128 snapshot files corresponding to redshifts ranging from $z = 17$ to 0.

The details regarding the GADGET-X and GIZMO-SIMBA codes used for the resimulation of clusters are as follows:

(i) **GADGET-X** : It is an updated, modified version of GADGET3 code (Murante et al. 2010; Rasia et al. 2015; Planelles et al. 2017) in which the evolution of dark matter is followed by the gravity solver

of the GADGET3 Tree-PM code, an updated version of GADGET2 code (Springel 2005). It incorporates an improved SPH scheme (Beck et al. 2016) with artificial thermal diffusion, time-dependent artificial viscosity, high-order Wendland C4 interpolating kernel, and wake-up scheme. Gas cooling for optically thin gas, accounting for metal contributions, is computed using the technique described in Wiersma, Schaye & Smith (2009). Additionally, a uniform ultraviolet (UV) background is incorporated following the approach described in Haardt & Madau (1996). Star formation in this work follows the approach described in Tornatore et al. (2007) and adopts the star formation algorithm presented by Springel & Hernquist (2003). This algorithm treats gas particles as multiphase, contributing to a self-regulating interstellar medium when their densities rise above a particular threshold. The star formation rate is determined solely by the gas density in this model. Stellar feedback, specifically SN feedback, is implemented as a kinetic energy-driven scheme, following the prescription in Springel & Hernquist (2003). Each star particle is treated as a single-stellar population (SSP), and the evolution of each SSP is modelled following the Chabrier (2003) stellar evolution prescriptions. The simulation takes into account metals from Type Ia and Type II SNe, as well as from asymptotic giant branch phases, tracking the evolution of 16 chemical species. The growth of black holes and the implementation of AGN feedback in GADGET-X are based on the refined model presented in Steinborn et al. (2015). In this model, super massive black holes grow via Eddington-limited Bondi–Hoyle-like gas accretion, with a distinction made between hot and cold components.

(ii) **GIZMO-SIMBA** It is based on the GIZMO cosmological hydro-dynamical code (Hopkins 2015) with its meshless finite-mass scheme and uses the physics of galaxy formation input from the state-of-the-art Simba simulation (Davé et al. 2019). The baryon model was recalibrated because the initial conditions of THE THREE HUNDRED have a lower-resolution than the original SIMBA simulation, and both simulations had different objectives (cosmological run for SIMBA and galaxy cluster for THE THREE HUNDRED). The GRACKLE-3.1 library (Smith et al. 2017) is used to implement the processes of radiative cooling, photon heating, and gas ionization. The spatially uniform UV background model (Haardt & Madau 2012) and the self-shielding prescription, based on the approach by Rahmati et al. (2013), are employed. Additionally, a H_2-based star formation model from MUFASA (Davé, Thompson & Hopkins 2016) is included. Star formation-driven galactic winds are implemented based on a decoupled two-phase model, drawing inspiration from MUFASA but incorporating an additional mass-loading factor derived from Anglés-Alcázar et al. (2017b). The chemical enrichment model tracks eleven elements with metals enriched from Type Ia and Type II SNe and asymptotic giant branch stars. The black hole accretion description is based on two models: the torque-limited accretion model for cold gas (Anglés-Alcázar et al. 2015, 2017a) and the hot gas accretion model based on Bondi (1952). It incorporates three AGN feedback modes: a kinetic subgrid model for both 'radiative mode' and 'jet mode' with bipolar ejections, and a kinetic X-ray feedback model following Choi et al. (2012). A more extensive discussion about the baryon model can be found in Davé, Thompson & Hopkins (2016); Davé et al. (2019); Cui et al. (2022).

Apart from differences in their models, it is crucial to note that the two codes have distinct objectives when comparing simulation outputs to observations. The GADGET-X simulation is tuned to accurately reproduce the gas properties and relations observed in the observations, such as the temperature–mass (T–M) and the integrated Sunyaev–Zeldovich decrement versus mass (Y–M) relations

Table 1. Host haloes and their associated sub-halo sample obtained from the GADGET-X simulated clusters data set. The meaning of each column is indicated in the header (See subsection 2.2 for further details). The information presented in the table pertains to sub-haloes that are located at distances less than $0.15R_{200c}$. Sub-halo mass threshold of $M_{sub} > 1.87 \times 10^{11}$ M$_\odot$ is used in the table to calculate the statistics.

z	N_{host} [M$_\odot$]	Median M_{200c} N_{2D}^{sub}	Median M_{sub}^{2D}[M$_\odot$]	Median N_{3D}^{sub}	Median M_{3D}^{sub}[M$_\odot$]	Median N_{2D}^{sub}	Total N_{3D}^{sub}	Total
0.394	90	1.18×10^{15}	10	3.87×10^{11}	3	4.11×10^{11}	857	287
0.194	180	1.21×10^{15}	9	4.00×10^{11}	3	4.20×10^{11}	1675	548
0	321	1.24×10^{15}	7	3.82×10^{11}	2	3.70×10^{11}	2551	832

(e.g. Li et al. 2020, 2023; Sayers et al. 2023). Alternatively, the GIZMO-SIMBA simulation is calibrated to reproduce the galaxy stellar properties, including the total stellar fraction, the satellite stellar mass function, and the brightest cluster group (BCG) halo mass functions (see Cui 2022; Zhang et al. 2022; Ferragamo et al. 2023, for comparisons between the two simulations). Since the introduction of the THE THREE HUNDRED project in Cui et al. (2018), several studies have used this data on many different projects, such as Ansarifard et al. (2020); Kuchner et al. (2020); Haggar et al. (2020a); Rost et al. (2021); de Andres et al. (2022). We refer the reader to these papers for more details about the project.

2.1 The halo and sub-halo catalogues

The simulation data are analysed using the AHF open-source software (Knollmann & Knebe 2009) to generate halo/sub-halo catalogues. AHF identifies structures hierarchically within cosmological simulations. It detects and locates spherical overdensity peaks in the density field of the simulation, consistently considering dark matter, stars, and gas particles. The physical properties of all identified haloes are determined on the basis of the gravitationally bound particles. Halo positions are determined by the peak of the highest density and the radius R_{200c}. Additionally, substructures, referred to as sub-haloes, are identified using the same process. Sub-haloes are smaller gravitationally bound entities located within the radius R_{200c} of a larger central structure termed the host halo.

AHF searches for connected overdensity regions within the radius R_{200c} of the main halo, considering these regions as potential sub-haloes. For each potential sub-halo, AHF determines whether the particles within the overdensity region are gravitationally bound to the main halo. This involves analysing and comparing the particles' velocities with the local escape velocity obtained using the spherical potential approximation. If the overdensity region is confirmed to be gravitationally bound to the main halo, it is identified as a sub-halo. In the following subsection, we will describe the selection procedure of our host haloes and their associated sub-haloes used in our study.

2.2 Host-halo and sub-halo sample selection

We selected the sample from each simulated cluster region (for both GADGET-X and GIZMO-SIMBA in the THE THREE HUNDRED data set), focusing on three particular redshifts: $z = 0.394$, $z = 0.194$, and $z = 0$. The choice of $z = 0.394$ allows for a close comparison with the observed galaxy clusters in M20, which have redshifts in the range $0.2 < z < 0.6$ with a median $z = 0.39$. The two additional redshifts are chosen for evolution studies. Host haloes with $M_{200c} > 9.59 \times 10^{14}$ M$_\odot$ are selected in each simulation region, ensuring that the uncontaminated mass fraction of high-resolution particles is greater than 0.98[4] This mass cut is chosen to cover the observed

cluster mass range. Note that the three cluster masses in M20 are 1.59 ± 0.36 (MACS J1206.2–0847), 1.04 ± 0.22 (MACS J0416.1–0403), and 2.03 ± 0.67 (Abell S1063) $\times 10^{15}$ M$_\odot$ (see table 1 in Bergamini et al. 2019).

For each host halo identified at three different redshifts in the simulation runs of the THE THREE HUNDRED project, we further made selections of sub-haloes with the two scenarios given below

(i) sub-haloes that are located within a projected distance of less than $0.15R_{200c}$ (where R_{200c} represents the radius of the host halo) from the host-halo centre in the simulation's XY plane, that is, $R_{2D} < 0.15R_{200c}$.

(ii) Sub-haloes that are physically located at a distance less than $0.15R_{200c}$ from their host-halo centre, that is, $R_{3D} < 0.15R_{200c}$. We first considered all sub-haloes outside of 2 per cent of R_{200c} from the cluster centre, approximately corresponding to the size of the BCG. This distance of $0.02R_{200c}$ is roughly 40 kpc, essentially matching the size of the BCG. Within this radius, the identification of the satellite galaxies in observations and sub-haloes in simulation (see Onions et al. 2012, for example) is challenging. Furthermore, these sub-haloes constitute only a small fraction (around 17 per cent for GADGET-X and about 3 per cent for GIZMO-SIMBA at each redshift) of our total sample. As such, we removed these sub-haloes near the centre of the cluster. To select well-resolved sub-haloes for correlation studies, a mass cut of $M_{sub} > 1.87 \times 10^{11}$ M$_\odot$ is applied to the data set. With our sub-halo mass threshold set at 1.87×10^{11} M$_\odot$ and, in addition, $M_{stellar} > 7.37 \times 10^{9}$ M$_\odot$, the total number of particles inside the sub-haloes for GADGET-X and GIZMO-SIMBA used in the correlation study exceeds 100. This was done to mitigate potential resolution-related issues that could affect the sub-halo's properties, which can be crucial for the later coefficient studies. We further refer to the appendix Section A for the convergence check. Similarly, we also eliminated any contaminated sub-haloes with a low-resolution particle mass fraction greater than 2 per cent. We have excluded sub-haloes that do not contain any stars from our analysis. This is because the study conducted by M20 uses galaxies as tracers of sub-haloes and hence it cannot detect these objects. Although completely dark sub-haloes could have a lensing effect in theory, most of the dark sub-haloes in the simulation have the lowest mass, which could be due to a resolution issue.

At redshifts $z = 0.394$, 0.194, and 0.0, GADGET-X consists of 0, 4, and 41 sub-haloes, respectively, within $0.15 R_{200c}$ in 3D with the stellar fraction, f_*, greater than 0.8. In contrast, for GIZMO-SIMBA, the number is zero at $z = 0.394$, 0.194, and 2 at $z = 0$. These sub-haloes may arise due to some artificial or numerical issues in the simulation, possibly connected to strong tidal stripping. Therefore, we also exclude them in our study. Nevertheless, excluding such a small fraction of substructures won't affect our results, especially for GIZMO-SIMBA.

General information on our chosen sample is presented in Tables 1 for GADGET-X and 2 for GIZMO-SIMBA. In Table 1, details on the selected host haloes with the mass cut are provided, including the number (N_{host}, column 2), the median mass M_{200c} (column 3) of host

---

[4] The fraction is not 100 per cent, for AHF takes BH particles as low-resolution particles. However, changing this fraction does not affect our results.

Table 2. Similar to Table 1, but for GIZMO-SIMBA.

z	N_{host}	Median M_{200c} [M$_\odot$]	Median N_{2D}^{sub}	Median M_{2D}^{sub}[M$_\odot$]	Median N_{3D}^{sub}	Median M_{3D}^{sub}[M$_\odot$]	Total N_{2D}^{sub}	Total N_{3D}^{sub}
0.394	82	1.19×10^{15}	15	3.57×10^{11}	6	3.61×10^{11}	1231	466
0.194	169	1.20×10^{15}	13	3.47×10^{11}	5	3.45×10^{11}	2297	914
0	302	1.23×10^{15}	11	3.39×10^{11}	5	3.27×10^{11}	3832	1520

haloes, the median number of sub-haloes within $R_{2D} < 0.15R_{200c}$ of each host halo (column 4) and $R_{3D} < 0.15R_{200c}$ (column 6) with their median masses in column 5 and 6, respectively. Additionally, the table also provides the total number of selected sub-haloes for $R_{2D} < 0.15R_{200c}$ (column 7) and $R_{3D} < 0.15R_{200c}$ (column 8) for GADGET-X simulated clusters. The different rows show these quantities at the three different redshifts. Similarly, Table 2 reports information for the selected host-haloes and sub-haloes for simulated clusters at three different redshifts for the GIZMO-SIMBA run. It is worth noting that GIZMO-SIMBA tends to have more sub-haloes than GADGET-X, which is examined and discussed later.

Based on this data set of simulated clusters' host-haloes and sub-haloes from THE THREE HUNDRED data set, we will commence our investigation to examine whether significant offsets exist between the observations of M20 and the simulations in the context of strong gravitational lensing.

3 SUB-HALO MASS FUNCTION

We begin our analysis by comparing the cumulative sub-halo mass functions predicted by the THE THREE HUNDRED clusters with the ones derived from the lens model of the three reference clusters, MACSJ0416, MACSJ1206, and AS1063, in M20. To accomplish this, we calculate the sub-halo mass function for each cluster, determining the median cumulative sub-halo mass function at specified redshifts for the GADGET-X and GIZMO-SIMBA simulations. This process involves utilizing the available sub-halo information associated with each cluster. Further, we bin the sub-haloes based on their mass, M_{sub}, into logarithmic mass bins and calculate the median value of $N(> M_{sub})$ for each bin. This procedure yields the median cumulative sub-halo mass function for the simulated clusters at the respective redshifts. Additionally, we calculate the lower and upper 34 per cent percentiles for $N(> M_{sub})$ in each logarithmic mass bin to quantify the associated uncertainty.

Fig. 1 illustrates the median cumulative sub-halo mass function $R_{2D} < 0.15R_{200c}$ (left) and $R_{3D} < 0.15R_{200c}$ (right) for both GADGET-X and GIZMO-SIMBA, at three redshifts, $z = 0.394$, $z = 0.194$, and $z = 0$. The grey-shaded region in Fig. 1 (left and right) represents the upper and lower 34 per cent quantiles for the cluster at redshift $z = 0.394$ for GADGET-X and GIZMO-SIMBA. Despite the distinct approaches used, whether considering the projected 2D distance or the actual physical 3D distance between sub-haloes and the host-halo centre, the cumulative sub-halo mass function follows a power-law trend when fitted analytically with a power-law function, as previously demonstrated in Giocoli, Tormen & Van Den Bosch (2008). The cumulative sub-halo mass function observed in the GIZMO-SIMBA simulation exhibits a pronounced straight power-law trend, with a power index nearly equal to 1 compared to the GADGET-X simulation. Upon comparing the results with the observed sub-halo mass functions from M20 obtained through a strong lensing model (represented by black curves with different line styles in Fig. 1), we observe consistency between the observations of MACSJ0416 and MACSJ1206 and the results

from GIZMO-SIMBA simulated clusters within $R_{2D} < R_{200c}$. For the GADGET-X simulated clusters, we find that the sub-halo mass function ($R_{2D} < 0.15R_{200c}$) has a better agreement with observation results for sub-halo masses greater than $\sim 1.18 \times 10^{11}$ M$_\odot$. Regarding the low sub-halo mass function at the low-mass end, its baryon model has a stronger resolution dependence[5] because its sub-halo mass function is closer to the power law if we don't apply the stellar mass constraint $M_* > 0$ (see also Contreras-Santos et al. 2023, who found many dark sub-haloes in GADGET-X.). We would like to emphasize that during our convergence analysis of the sub-halo mass functions, see Appendix A, from both GADGET-X and GIZMO-SIMBA, without imposing any constraints, the two simulations generally exhibit agreement with each other for $M_{sub} > 1.47 \times 10^{11}$ M$_\odot$. However, a discrepancy persists for $M_{sub} < 1.47 \times 10^{11}$ M$_\odot$, with the sub-halo mass function of GIZMO-SIMBA being higher compared to GADGET-X. This discrepancy is a key reason for restricting our correlation investigations to sub-haloes with a mass higher than this cut. It is believed that the strong SN feedback is the cause for this deviation at $M_{sub} < 1.47 \times 10^{11}$ M$_\odot$. This is because the low-mass haloes have a shallower potential, the SN feedback can expel gas from galaxies to stop their star formation. However, note that the gas in these sub-haloes can also be quickly stripped away in and around cluster environment (Arthur et al. 2019). Therefore, the SN feedback should mostly affect the galaxy properties before the infall. A more prominent impact of gas stripping can result in the depletion of all gas from the haloes, thereby eliminating SN feedback due to the absence of star formation.

The right panel of Fig. 1 highlights the projection effect, leading to an increase in sub-halo numbers by a factor of ~ 2.5, regardless of sub-halo masses. Although we focus on sub-haloes within R_{200c} of the host halo in this study, we verified that the sub-halo mass function is only underestimated by approximately 2.21 per cent compared to when a much larger line-of-sight project distance, $2.5R_{200c}$, is used. This is simply because there are much fewer galaxies/sub-haloes at outer radius (see Li et al. 2020, 2023, for example). Therefore, using a slightly larger projection distance will not impact our results. Alternatively, the observed sub-halo mass function for the three reference clusters exhibits a decline in the lower-mass range ($\approx 8.85 \times 10^{10}$ M$_\odot$), which is likely attributed to limitations in the detection of substructures in the observation. Quantifying this observational completeness limit for the cluster galaxies in terms of mass is not straightforward, as it depends on the apparent magnitude of the observation, with the typical selection limit being $m_{F160W} < 24$. Lastly, there is a weak redshift evolution of the sub-halo mass functions in all the simulation samples (see also Giocoli et al. 2008; Giocoli et al. 2010), which we will detail in the following subsection.

---

[5]Though we show the sub-halo mass function down to $\sim 1.47 \times 10^{10}$ M$_\odot$, it is worth noting that these sub-haloes only have around 10 dark matter particles.
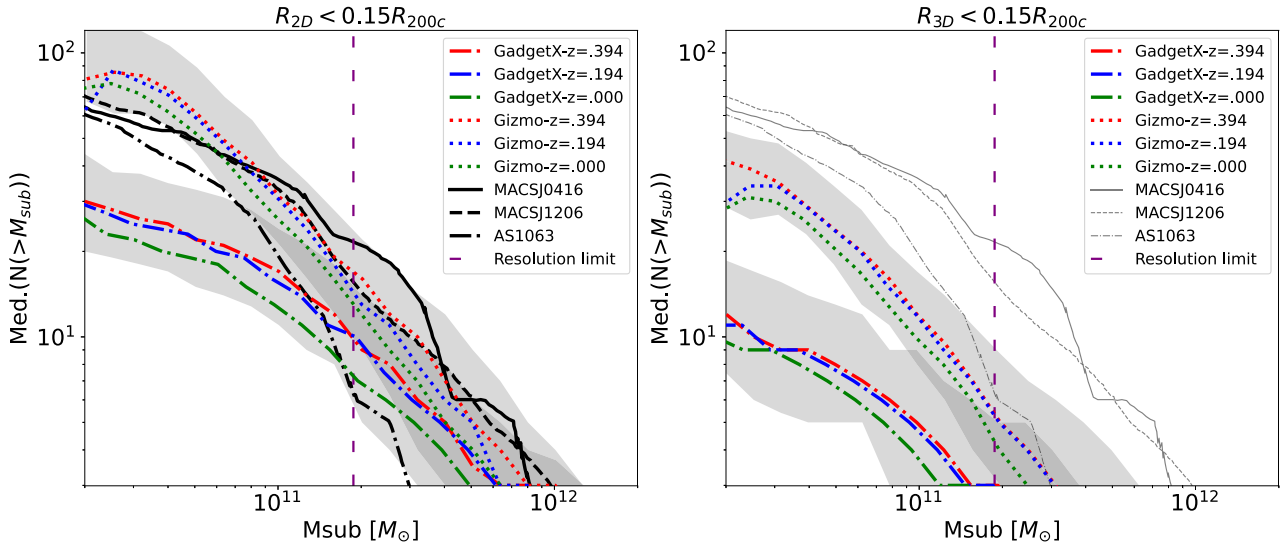
Figure 1. The cumulative sub-halo mass function is presented for two cases: the 2D projected constraint with $R_{2D} < 0.15R_{200c}$ (left) and the spatial 3D constraint with $R_{3D} < 0.15R_{200c}$ (right). The dotted line style represents the GIZMO-SIMBA simulation results, while dash-dot lines show median cumulative sub-halo mass functions from GADGET-X. The shaded areas show the 16th−84th percentiles from all clusters at $z = 0.394$. The mass functions of sub-haloes in GADGET-X and GIZMO-SIMBA simulations are displayed for three redshifts: $z = 0.394$ (red), $z = 0.194$ (blue), and $z = 0$ (green). The projected results on the left panel used all sub-haloes located within a projected 2D distance of $0.15R_{200c}$, that is, $R_{2D} < 0.15R_{200c}$. Alternatively, the right panel illustrates the results using only sub-haloes situated within a physical 3D distance of R_{200c}, that is, $R_{3D} < 0.15R_{200c}$. In both panels, the same observed sub-halo mass functions from three reference clusters in M20 are presented with black curves with different line styles; see the legend for details. The purple dashed line denotes the sub-halo mass cutoff, which is set at 1.87×10^{11} M$_\odot$ and corresponds to the resolution limit.

3.1 The redshift evolution of the sub-halo mass function

The clusters observed in M20 are not closely centred around a redshift of approximately $z = 0.4$; instead, they span a range of redshifts, with the lowest at $z = 0.234$ and the highest at $z = 0.58$. Meanwhile, including the result at $z = 0$ is also interesting because most of the comparisons between simulations and observations are done at $z = 0$. To investigate the observed simulation discrepancy, the study, for simplicity, examined the redshift evolution of the sub-halo mass function by considering host halo samples from the simulation at $z = 0.394$, as well as at $z = 0.194$ and $z = 0$. It is expected that more massive clusters will host a greater number of sub-haloes. As shown in Table 1 and Table 2, the median halo mass slightly increases as the redshift decreases for both GADGET-X and GIZMO-SIMBA. One should expect a higher sub-halo mass function at $z = 0$ than $z = 0.394$. However, the results in Fig. 1 for both GADGET-X and GIZMO-SIMBA and within both R_{2D} and R_{3D} show an opposite evolution, that is, a lower (fewer sub-haloes) sub-halo mass function at $z = 0$ compared to $z = 0.394$. We suspect that this could be due to the different halo mass distributions between these redshifts. Therefore, we further investigate this aspect in this subsection.

To explore the redshift evolution of the sub-halo mass function, we focus on presenting the 2D projected results, which can be more directly compared to observations. It is worth noting that the results for R_{3D} are comparable to those for R_{2D}. The cumulative sub-halo mass function for all GADGET-X and GIZMO-SIMBA simulated clusters at $z = 0.349$ is shown in the first column of Fig. 2, with line colours indicating the cluster mass, as specified by the colour bar on the right. To highlight the residual redshift evolution of the sub-halo mass function, we first performed a normalization step by dividing each host halo's cumulative sub-halo mass function by its own halo mass. This normalization step eliminates any host halo mass

dependence from the cumulative sub-halo mass distribution. We then proceed with the calculation of the median sub-halo mass function by grouping the normalized sub-halo mass in logarithmic mass bins and then calculating median $N(>M_{sub})/M_H$ in each bin. The right panel of Fig. 2 shows the redshift evolution of the normalized sub-halo mass distribution predicted by the simulations for both GADGET-X and GIZMO-SIMBA. The plot clearly illustrates the evolution of the sub-halo mass function as the redshift decreases from $z = 0.349$ to $z = 0$. The figure shows that, within a given parent halo, a greater number of sub-haloes are expected to be observed at earlier times. This similar inference about the redshift evolution of the sub-halo mass function aligns with the findings presented in Gao et al. (2004) and Gao et al. (2011). However, here we notice that the evolution we observed in our hydrodynamical simulations is milder compared to the earlier studies of dark matter-only simulations. This observation is further supported by the median N_{2D}^{sub} and median N_{3D}^{sub} columns in Tables 1 and 2, respectively. Moreover, upon examining Table 2 for GIZMO-SIMBA, we observe a general decreasing trend in the median sub-halo mass (check M_{sub}^{2D} and M_{sub}^{3D} from redshift $z = 0.394$ to $z = 0$). This is consistent with the evolutionary trend for the sub-halo mass function shown in Fig. 1. The explanation of this, we speculate, lies in two aspects (i) the pseudo-halo mass evolution (see Diemer, More & Kravtsov 2013; Sembolini et al. 2013, for example) due to the halo mass being based on the universe's critical overdensity. As such, the comoving $R_{200c}(z = 0) < R_{200c}(z = 0.4)$, of which volume at higher redshift slightly increases, that is, include more substructures. (ii) the thermalization and stabilization of galaxy clusters after $z \approx 0.3$ (Sereno et al. 2021). Before that redshift, clusters still actively grow through mergers. After it, the growth mostly halts with the infalling substructures slowly getting dissolved or merging into the central galaxy, which results in fewer substructures and a lower sub-halo mass function.
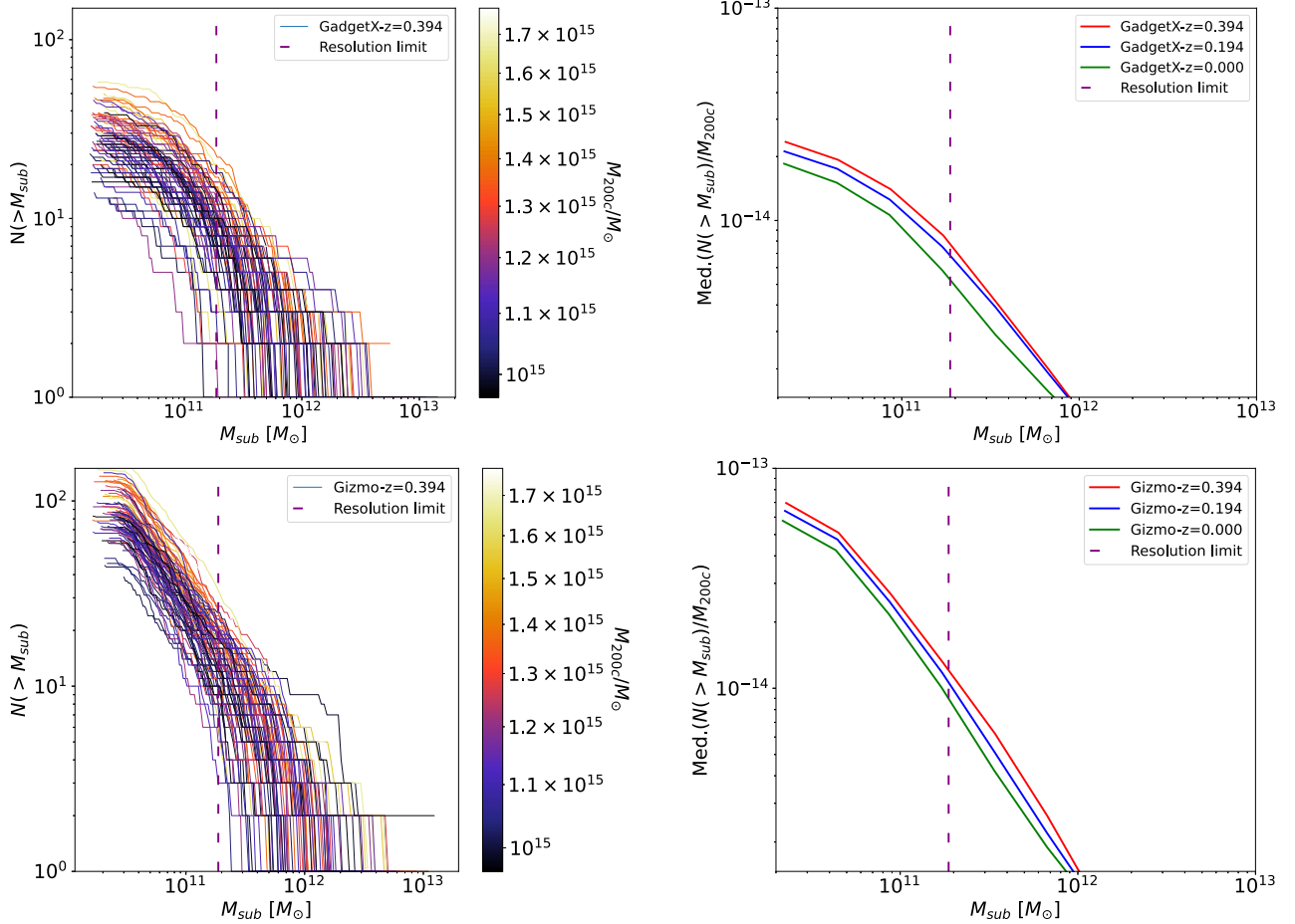
Figure 2. In the left column, we illustrate the un-normalized sub-halo mass functions at $z = 0.394$ for both GADGET-X and GIZMO-SIMBA, demonstrating their dependence on halo mass. The right column of the above figure displays the corresponding cumulative sub-halo mass functions for the normalized sub-halo mass function at redshift $z = 0.394$, along with the normalized sub-halo mass functions at $z = 0.194$ and $z = 0$. The purple dashed vertical line indicates the sub-halo mass threshold of 1.87×10^{11} M$_\odot$ for both GADGET-X and GIZMO-SIMBA, corresponding to the resolution limit.

4 CUMULATIVE SUB-HALO $V_{\rm CIRC}$ FUNCTION

In this section, we calculate and compare the cumulative sub-halo $V_{\rm circ}$ function for both the GADGET-X and GIZMO-SIMBA simulations at three different redshifts: $z = 0.394$, $z = 0.194$, and $z = 0$. To estimate each sub-halo $V_{\rm circ}$ in both GADGET-X and GIZMO-SIMBA simulations, we utilized the output profiles generated by AHF (Knollmann & Knebe 2009). The AHF output files contain radial profiles for various halo/sub-halo properties, such as mass, density, rotation curve, escape velocity, etc. Here, we specifically used the rotation curve of each sub-halo to estimate $V_{\rm circ}$ in both GADGET-X and GIZMO-SIMBA at the three redshifts. The circular velocity, denoted as $V_{\rm circ}$, for a sub-halo is determined by identifying the maximum circular velocity at radii beyond the convergence limit, dominated by two-body collisions according to the criterion of Power et al. (2003). The rotation curve for halo/sub-halo is calculated inclusively considering both baryons and dark matter particles in the AHF profile file. We have verified that this value is compatible with the one in the AHF halo properties.

The sub-halo $V_{\rm circ}$ function is computed for each host cluster to determine the median cumulative sub-halo $V_{\rm circ}$ function at the specified redshifts for both GADGET-X and GIZMO-SIMBA simulations. To calculate the median sub-halo $V_{\rm circ}$ function, we interpolate the individual sub-halo $V_{\rm circ}$ functions for each host halo at given $V_{\rm circ}$

values, and then calculate the median value of $N(> V_{\rm circ})$ using all the interpolated profiles. This process yields the median cumulative sub-halo $V_{\rm circ}$ function for the simulated clusters at the respective redshifts.

Fig. 3 illustrates the median cumulative sub-halo $V_{\rm circ}$ function for both GADGET-X and GIZMO-SIMBA simulations at three different redshifts: $z = 0.394$, $z = 0.194$, and $z = 0$. The left panel shows the function for $R_{\rm 2D} < 0.15R_{\rm 200c}$, while the right panel presents it for $R_{\rm 3D} < 0.15R_{\rm 200c}$. In Fig. 3, the shaded grey region represents the upper and lower 34 per cent percentiles for clusters at redshift $z = 0.394$ in both GADGET-X and GIZMO-SIMBA simulations. The $V_{\rm circ}$ functions for GIZMO-SIMBA are higher compared to GADGET-X for both $R_{\rm 2D} < 0.15R_{\rm 200c}$ and $R_{\rm 3D} < 0.15R_{\rm 200c}$. Once again, we observe that the projection effect leads to an approximately two-fold increase in the sub-halo count in both the GADGET-X and GIZMO-SIMBA simulations. As expected, the $V_{\rm circ}$ function is very similar to the sub-halo mass function shown in Fig. 1. Additionally, we note a subtle redshift evolution in the cumulative sub-halo $V_{\rm circ}$ function for both GADGET-X and GIZMO-SIMBA which aligns with the result of the sub-halo mass function considering the positive correlation between $V_{\rm circ}$ and $M_{\rm sub}$, further discussed later. Investigating the $V_{\rm circ}$ function will provide more insight views of the $M_{\rm sub}$–$V_{\rm circ}$ relation.
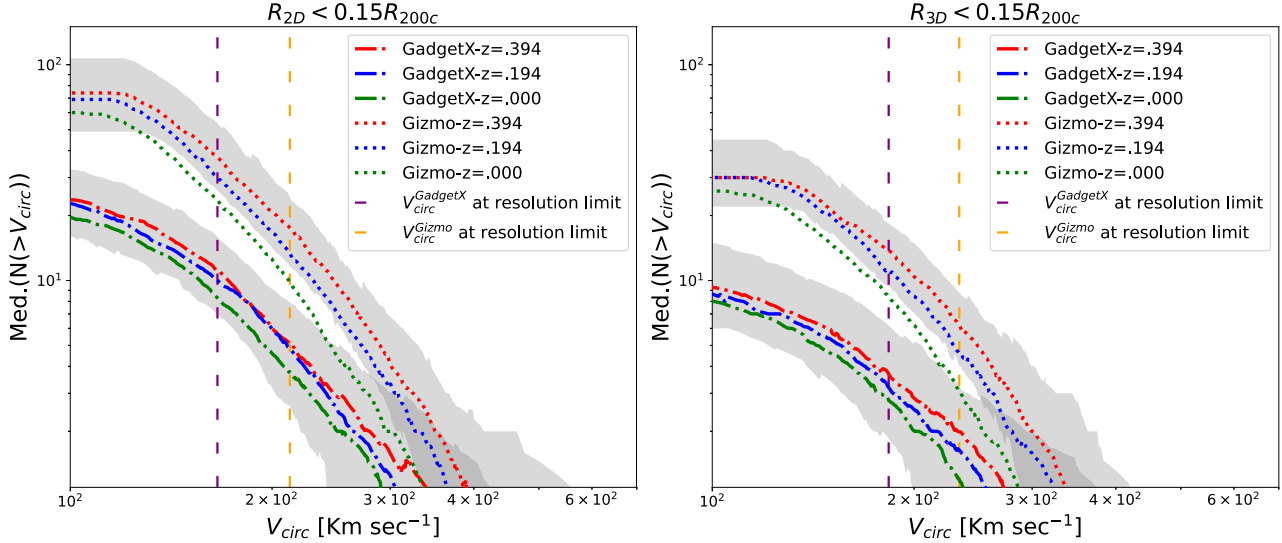
Figure 3. The projected (left panel) and spatial 3D (right panel) cumulative sub-halo V_{circ} functions. The dotted line style represents the GIZMO-SIMBA simulation results, while dash-dot lines show median cumulative sub-halo V_{circ} functions from GADGET-X. The shaded areas show the 16th–84th percentiles from all clusters at $z = 0.394$. The V_{circ} functions of sub-haloes in GADGET-X and GIZMO-SIMBA simulations are displayed for three redshifts: $z = 0.394$ (red), $z = 0.194$ (blue), and $z = 0$ (green). To calculate the V_{circ} functions for both GADGET-X and GIZMO-SIMBA, we considered sub-haloes with $M_{sub} > 1.47 \times 10^{10}$ M$_\odot$. The vertical dashed lines in Fig. 3 indicate the resolution limit V_{circ} values for both GADGET-X (purple) and GIZMO-SIMBA (yellow) by the mass cut at 1.87×10^{11} M$_\odot$ at $z = 0.394$ in previous plots. These V_{circ} value at the resolution limit 1.87×10^{11} M$_\odot$ for GADGET-X and GIZMO-SIMBA is obtained from the $M_{sub}-V_{circ}$ relation (Fig. 4) for $z = 0.394$, respectively.

5 $M_{\rm SUB}-V_{\rm CIRC}$ RELATION

In this section, we investigate the discrepancy between the concentration of sub-haloes in THE THREE HUNDRED simulations and the lensing results of M20. Following M20, Bahé (2021); Ragagnin et al. (2022), we employed the $M_{sub}-V_{circ}$ relationship as a metric to infer the concentration of sub-haloes within the clusters. The sample of selected sub-haloes for both GADGET-X and GIZMO-SIMBA remains unchanged. To derive the $M_{sub}-V_{circ}$ relationship, we initially divide the sub-halo masses into logarithmic mass bins and subsequently calculate the median V_{circ} for each respective bin. $M_{sub}-V_{circ}$ relation is then obtained by plotting the central value of M_{sub} of each bin with respect to the corresponding median values of V_{circ} for each bin. This procedure was repeated for both GADGET-X and GIZMO-SIMBA simulations at the three redshifts considered in our study.

In Fig. 4, we present the $M_{sub}-V_{circ}$ relationship for the sub-haloes from GADGET-X and GIZMO-SIMBA simulated clusters and compare it with the relation of the observed clusters derived by M20. The left panel of Fig. 4 presents the projected results while the right panel shows the 3D case. We use different colours to show the the $M_{sub}-V_{circ}$ relations (for both GADGET-X and GIZMO-SIMBA) at three different redshifts, namely $z = 0.394$, $z = 0.194$ and $z = 0$. When sub-haloes follow the distance constraint $R_{2D} < 0.15R_{200c}$, both GADGET-X and GIZMO-SIMBA simulated clusters exhibit consistently lower V_{circ} values compared to the fitting line from observation. Sub-haloes located at the periphery (i.e. $R_{3D} \approx R_{200c}$) for the 2D case, cause the simulation's $M_{sub}-V_{circ}$ relation to fully shift downward compared to the 3D case. GIZMO-SIMBA, though, shows slightly higher V_{circ} than GADGET-X. Furthermore, GIZMO-SIMBA exhibits a weak redshift evolution with higher V_{circ} at $z = 0.394$ compared to $z = 0$, whereas no redshift evolution is observed in GADGET-X. Similarly, the same conclusions are reached for the case when $R_{3D} < 0.15R_{200c}$, albeit that both seem to become closer to the observation fitting line, which is in agreement with M20 and our later correlation studies. Even after

considering the sub-haloes of the 10 most massive host haloes, the discrepancy between the observed and simulated V_{circ} values persists. We do not see significant differences between different sub-halo masses regarding the distances to the fitting line, although the shaded regions seem larger, thus closer to the fitting line, at higher sub-halo masses. We also emphasize that the disparity between the $M_{sub}-V_{circ}$ relations of GADGET-X and GIZMO-SIMBA is primarily limited to the lower sub-halo mass range. As we have noticed, the sub-haloes with a lower halo mass, below the vertical-dashed line, can be unresolved. As presented in Fig. 4, there is no clear deviation from the anomalous trend at or around the mass cut, actually all the way up to $\sim 10^{12}$ M$_\odot$. This suggests that the influence of simulation resolution should be either minor for this $M_{sub}-V_{circ}$ relation or systematical, that is, a constant shift of this relation regardless the sub-halo mass.

Nevertheless, we acknowledge that further investigations with higher resolution simulations are necessary to gain a more complete insight into how unresolved sub-haloes in this mass range might affect the relation, though the initial comparison with a few high-resolution clusters does not reveal any clear changes. We also observed that the simulated $M_{sub}-V_{circ}$ relationship for sub-haloes with masses $M_{sub} \lesssim 1.47 \times 10^{11}$ M$_\odot$, which is the most crucial mass range for GGSL events (Ragagnin et al. 2022), differs constantly from observations. Conversely, the $M_{sub}-V_{circ}$ relation in simulations for the massive sub-haloes, $M_{sub} > 5.90 \times 10^{11}$ M$_\odot$, becomes closer to the observed relation by varying the baryon parameters, as noted also in Bahé (2021). However, it's worth noting that this specific range of sub-halo masses is notably higher than what is observed, as highlighted in Ragagnin et al. (2022). Though we have a much larger sample and observe that the lines are closer to the observation line at the most massive sub-halo mass range, the discrepancy at the low sub-halo mass end remains unsolved. Note that the resolution, which could affect this statement for our simulations, given by the checks from Ragagnin et al. (2022), Bahé (2021) and our examinations of the high-resolution the300 clusters, does not significantly impact
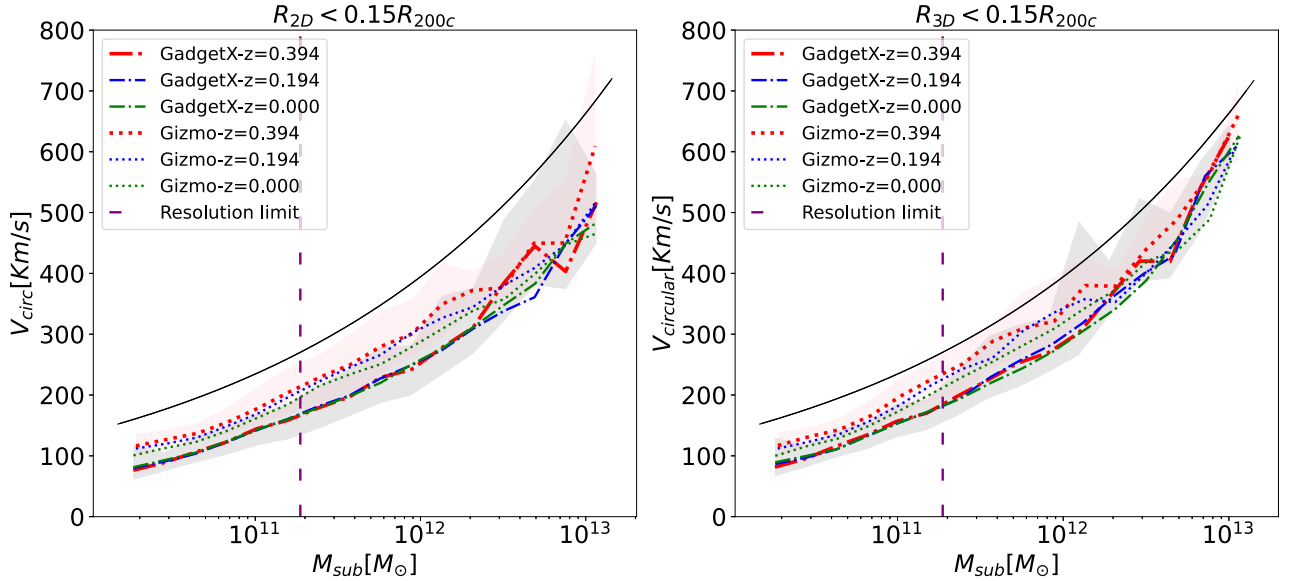
Figure 4. The relationship between sub-halo mass (M_{sub}) and maximum circular velocity (V_{circ}) for the 2D projected sub-haloes on left panel and for the 3D one on the right panel. The black solid line is observed fitting relation from M20 in both panels for reference. The M_{sub}–V_{circ} relation for the two simulations is distinguished by distinct line styles, with dashed-dot representing GADGET-X and dotted representing GIZMO-SIMBA. The M_{sub}–V_{circ} relation in GADGET-X and GIZMO-SIMBA simulations are displayed for three redshifts: $z = 0.394$ (red), $z = 0.194$ (blue), and $z = 0$ (green). The light grey and red shaded regions depict the upper and lower 34 per cent quantile regions computed in each logarithmic mass bin at redshift $z = 0.394$ for GADGET-X and GIZMO-SIMBA, respectively. The purple dashed line represents the sub-halo mass cutoff of $1.87 \times 10^{11}\,\mathrm{M_\odot}$, which is the limit for later Spearman correlation analysis.

the M_{sub}–V_{circ} relation. Therefore, it is still unclear whether this can be solved by high-resolution simulations without varying the baryon models. Alternatively, the difference between GIZMO-SIMBA and GADGET-X suggests that the baryon model may be the key in solving this issue. In the following section, we aim to investigate the influence of sub-halo properties on the M_{sub}–V_{circ} relation, where we examine how these properties relate to the difference between the V_{circ} obtained from the simulation and the one derived from observed fitting relations. This difference serves as a measure of the goodness-of-fit to the M_{sub}–V_{circ} relation.

5.1 The effects of the sub-halo properties on M_{sub}–V_{circ} relation

While GIZMO-SIMBA appears to be somewhat closer to the observed fitting line than GADGET-X, the deviation from the observational results remains substantial. This is particularly pronounced in the case of the projected data, which holds greater importance in the observational context. It is interesting to see that different baryon models indeed give slightly different results, which means there may be a cure for this discrepancy by better calibrating the baryon models. Therefore, in order to understand the impact of sub-halo properties on the M_{sub}–V_{circ} relation, we perform a Spearman correlation analysis between the different physical properties of the sub-haloes and the residual for all sub-haloes in the $R_{2D} < 0.15R_{200c}$ case. The Spearman correlation test involves converting the data into ranks and then calculating the correlation between the ranks of the two variables. This Spearman correlation analysis between the different physical properties of the sub-haloes and the residual not only provides more statistics but also presents a consistent comparison to the observation result. The residual ds is determined for each sub-halo by calculating the difference between its simulated circular velocity, V_{circ}^{sim}, and the circular velocity predicted by a fitting line (based on the M_{sub}–V_{circ} relation from M20 reference clusters) according to its sub-halo mass,

denoted as V_{circ}^{fit}. This difference is then normalized by the predicted circular velocity

$$ds = \frac{V_{circ}^{sim} - V_{circ}^{fit}}{V_{circ}^{fit}}. \qquad (1)$$

Note that, we only use sub-haloes with $M_{sub} > 1.87 \times 10^{11}\,\mathrm{M_\odot}$ to calculate these correlation coefficients. This is attributed to the potential influence of simulation resolutions on certain sub-halo properties, as sub-haloes below this range roughly consist of fewer than 100 dark matter particles. Apart from identifying haloes and their corresponding sub-haloes, AHF (Knollmann & Knebe 2009) also provide many physical properties associated with them. Here, we investigate these quantities which should have the most effects on the M_{sub}–V_{circ} relation. The sub-halo properties analysed with the Spearman correlation test include the Bullock Spin parameter, which is a measure of the spin of the sub-halo based on Bullock et al. (2001). It is calculated as $|J|/\sqrt{2}MRV$, where $|J|$ denotes the angular momentum, M is the mass of the sub-halo, R is the virial radius, and V is the virial circular velocity given by $V = \sqrt{\frac{GM}{R}}$. The measurements of J, M, and V are all confined to the virial radius R. This makes this spin definition especially attractive since it solely depends on the material within R, enabling its calculation for individual components. Hence, using this definition, the radial distribution of the spin is straightforward.

Furthermore, the analysis takes into account the baryonic mass fraction (f_b), which represents the proportion of baryonic matter (ordinary matter i.e. gas and stellar content) within the sub-halo. The centre-of-mass offset parameter (COM_offset), the distance between the centre of mass of the sub-halo and its density peak, is also considered. This is normally used as an indicator of the object's dynamical state (see Cui et al. 2017; Haggar et al. 2020b; De Luca et al. 2021, for example).
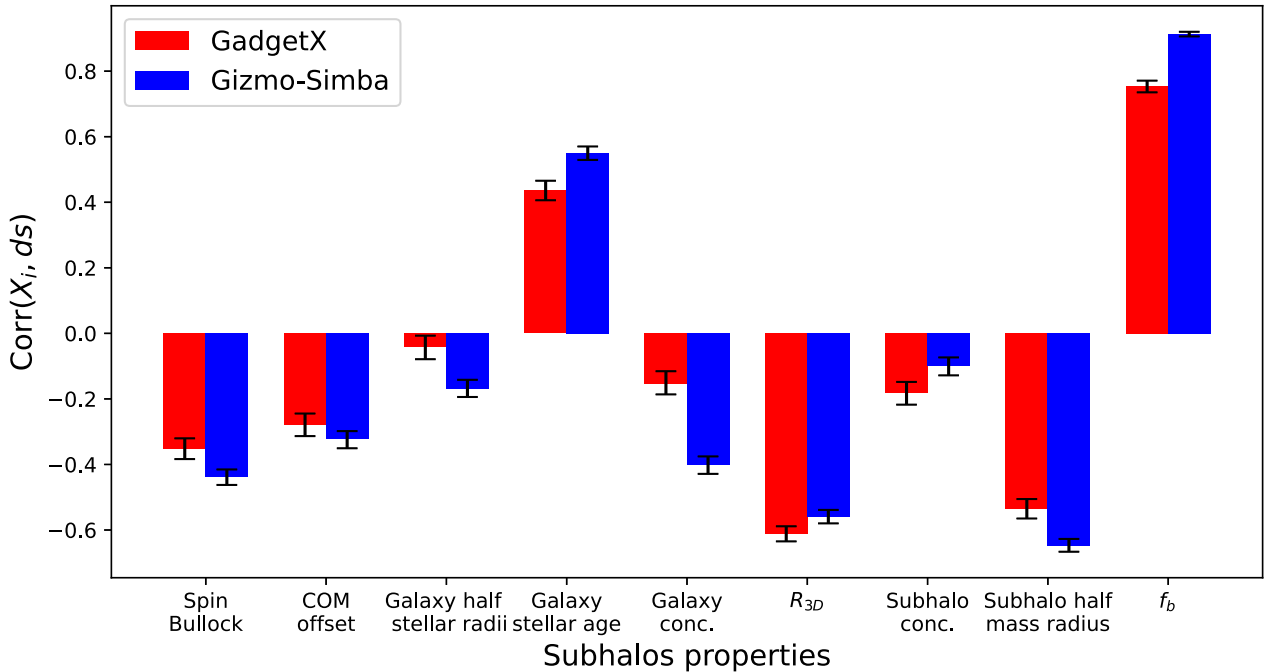
Figure 5. The Spearman correlation coefficient between the physical properties of sub-haloes and the residuals ds. The residual ds is computed as the distance from the sub-halo's circular velocity obtained from the simulation to the one predicted by the observed relation. To distinguish between the two simulations, we use the red bar plots for the results of GADGET-X and the blue bar plots for the results of GIZMO-SIMBA, respectively. The values of the bar plot are the Spearman correlation coefficient between the sub-halo residual ds and various sub-halo properties. Corr(X, ds) defines the Spearman correlation coefficient between the physical property X of sub-haloes and the residual ds. This parameter is obtained by rank-ordering the sub-halo property X and the residual ds, and then calculating the Pearson coefficient based on this rank-order list. The value of this parameter falls between –1 and 1. For the Spearman correlation studies, we chose sub-haloes that meet the following criteria: their mass $M_{sub} > 1.87 \times 10^{11}\,M_\odot$, and their 2D projected distance $R_{2D} < 0.15R_{200c}$. The Spearman correlation coefficients for each sub-halo property are accompanied by their respective upper 84 per cent and lower 16 per cent uncertainties.

In addition to that, we further calculate some galaxy and sub-halo properties that may be directly linked to the ds, but not provided by AHF. These properties included in the analysis are the physical distance between the host-halo and the sub-haloes (R_3D), the galaxy's half-stellar mass radii, the galaxy's stellar age, which is the mass-weighted mean of all-star particles within the half-stellar mass radius, the sub-halo half-mass radii, and the galaxy/sub-halo concentrations. As it is very difficult to decide the density profiles for these sub-haloes and therefore to estimate their concentration, it is very common to use the ratio of two radii, R_{80} and R_{20}, as an indicator of the concentration. Here, R_{80} marks the radius where 80 per cent of the total (stellar) mass of the sub-halo (galaxy) is included. With a similar definition for R_{20}, one would expect a more concentrated density profile should have a higher ratio R_{80}/R_{20}.

The correlation between the physical properties of the sub-haloes (for both GADGET-X and GIZMO-SIMBA) and the residual ds is depicted in Fig. 5. It is clear that both simulations generally agree on the (anti)correlation between ds and sub-halo/galaxy properties. Namely, the higher Spin, COM offset, galaxy/sub-halo half mass radius and concentrations, and a larger distance from the cluster centre, the further distance is to the fitted $M_{sub}-V_{circ}$ relation. Although it is not displayed in Fig. 5, the Peebles Spin parameter (Peebles 1969) also showed a similar anticorrelation trend and a correlation coefficient comparable to that of the more robust Bullock Spin parameter. At the same time, the older galaxy age (formed earlier) and sub-halo's baryonic mass fraction will bring the simulated sub-halo V_{circ} closer to the observed relation. We also examined the correlation trend for the stellar mass fraction, which exhibits a positive correlation

with the residual ds. It displayed a closely similar magnitude to the baryon fraction. This is not surprising given that simulated satellites have virtually no gas; therefore, these two fractions are expected to be nearly identical. It is worth noting that the most significant sub-halo properties are galaxy stellar age, R_{3D} distance, sub-halo half mass radius, and baryon fractions. The Spearman correlation trends between ds and R_{3D}, as well as ds and f_b, obtained from our analysis, have also been reported in M20 and Bahé (2021), respectively. The positive correlation between ds and galaxy age suggests early-galaxy formation in simulations will provide a better agreement, which is also consistent with the recent *JWST* observations on the very high-redshift galaxies (see Finkelstein et al. 2022; Naidu et al. 2022, for example). It is also interesting to note that in the GIZMO-SIMBA simulation, both the gas fraction (f_b) and galaxy age are more strongly positively correlated to ds compared to GADGET-X. For the negative correlation between ds and the sub-halo half mass radius, it is very easy to understand: the larger the radius, the puffier the sub-halo is, therefore, the lower V_{circ}. Naively, we also expect that the sub-halo half mass radius will be anticorrelated with the sub-halo concentration. By directly looking at the coefficient between the sub-halo half mass radius and concentration, which is also negatively correlated, we suspect that this is caused by different sub-halo masses for the anticorrelation at a fixed sub-halo will be diluted by plotting all the sub-haloes together. Therefore, we state that the mentioned correlation between sub-halo half mass radius and concentration is not shown in Fig. 6. Furthermore, this is also applied to the galaxy concentration parameter. We also emphasize that this correlation study should not be affected by the resolution effect with
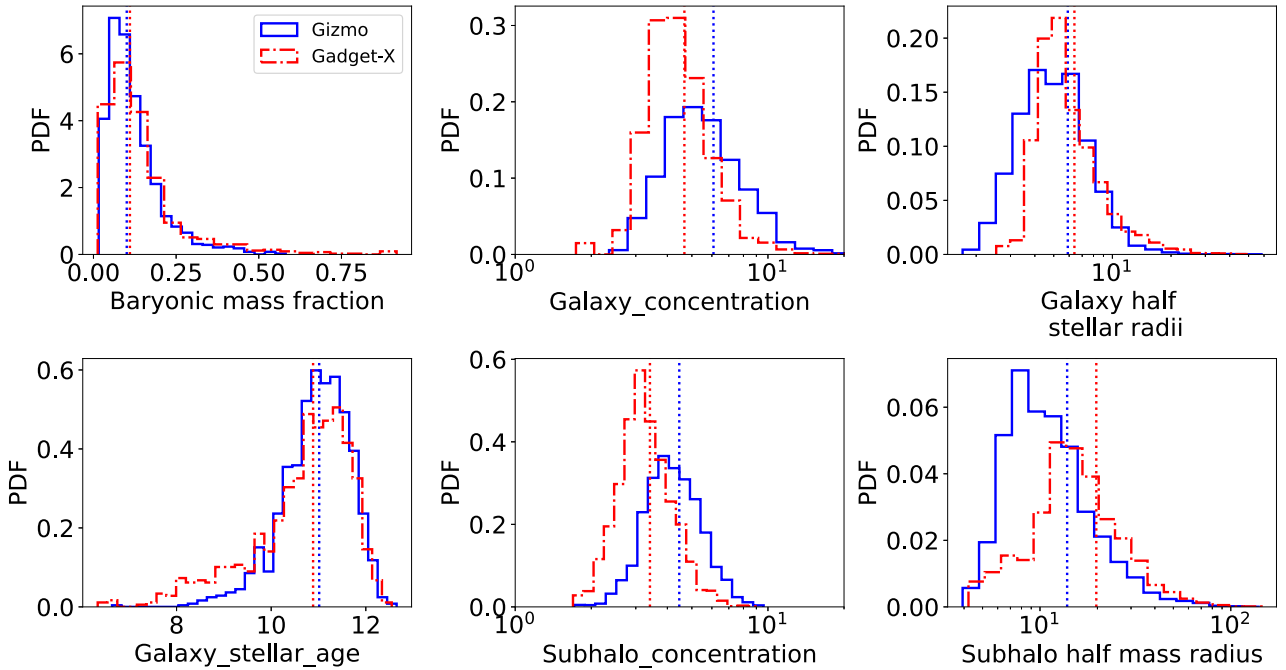
Figure 6. The probability density functions (PDFs) of the baryonic mass fraction, galaxy concentration, galaxy half stellar radii, galaxy stellar age, sub-halo concentration, and sub-halo half mass radii from top left to bottom right for both GADGET-X (red dash-dot steps) and GIZMO-SIMBA (blue solid steps). The distributions are presented in either linear or logarithms based on their spread ranges. The dotted vertical lines in each plot correspond to the median values of the distributions. For the comparison of sub-halo properties between the two simulations, we selected sub-haloes that meet the following criteria: their mass, $M_{sub} > 1.87 \times 10^{11}$ M$_\odot$, and their 2D projected distance, $R_{2D} < 0.15R_{200c}$.

sub-haloes above this mass limit $M_{sub} > 1.87 \times 10^{11}$ M$_\odot$. However, no definitive conclusions can be drawn regarding the influence of sub-halo properties on the M_{sub}–V_{circ} relation for sub-haloes falling below the mentioned mass threshold.

In addition to examining the correlations with ds, which highlights the effect of individual sub-halo properties, we also compared the distribution of sub-halo properties between GADGET-X and GIZMO-SIMBA in Fig. 6. The distributions of galaxy/sub-halo properties are presented with the 1D PDFs for both simulations. Through these comparisons, we expected to further understand the model differences between the two simulations and how they impact the M_{sub}–V_{circ} relation. In Fig. 6, only six interesting and important sub-halo properties are picked to show.

First, the sub-haloes in the simulated clusters of GADGET-X contain a marginally higher amount of baryonic content compared to those in GIZMO-SIMBA. Note that the distribution difference is larger when including low-mass sub-haloes. The positive correlation illustrated in Fig. 5 indicates that as the baryon fraction increases, the simulation's M_{sub}–V_{circ} relation aligns more closely with the observed fitting relation. The explanation behind this is that the inclusion of baryons through tidal stripping leads to an observed offset towards higher V_{circ} values in the M_{sub}–V_{circ} relation (Bahé 2021), which is also supported by the presence of sub-haloes with increased baryonic content results from the removal of dark matter in galaxies with the stellar mass is largely preserved (Armitage et al. 2019; Bahé et al. 2019; Joshi et al. 2019). However, this result seems to contradict the conclusion that GIZMO-SIMBA is closer to the fitting line than GADGET-X while their baryon fractions are very similar. We suspect the baryon fraction is only a sufficient condition, not a necessary condition to bring up the V_{circ}. The stellar mass fraction, though not shown in Fig. 6, follows a similar distribution as the baryon mass fraction. Similar to the

baryon fraction, the galaxy age distributions between GADGET-X and GIZMO-SIMBA are also very similar with a slight excess of young galaxies in GADGET-X. Therefore, the similarity of the two sub-halo properties between GADGET-X and GIZMO-SIMBA indicates that other quantity differences are the key to explaining the differences in the M_{sub}–V_{circ} relation. They are the sub-halo/galaxy half-mass radii and concentrations: it is clear that GIZMO-SIMBA has smaller half-mass radii, thus a higher concentration of both galaxy and sub-halo compared to GADGET-X. This is in agreement with Meneghetti et al. (2023), which found that the GGLS signal is also higher in GIZMO-SIMBA than GADGET-X, albeit that is still about a few times lower than observation. To boost the V_{circ}, as well as the GGLS signal, we will need even more compact sub-haloes/galaxies. To achieve that goal, we suspect an even earlier galaxy formation may bring the simulation closer to observation.

5.2 Global cluster properties impact on M_{sub}–V_{circ} relation

The next step in our analysis is to investigate the influence of the global properties of the host halo on the M_{sub}–V_{circ} relationship. This investigation is to provide some hints on whether the selected clusters in observation are biased or not. To determine any potential impact, we provide a similar study on the Spearman coefficient between the physical properties of the host haloes and the global residual $\overline{ds}$. Here, the global residual $\overline{ds}$ for each host halo is computed by averaging all its sub-haloes' ds, which are measured in the previous section.

In Fig. 7, we show the coefficient between $\overline{ds}$ and these four selected cluster properties: cNFW, Bullock spin parameter, COM offset, and total baryon fractions. Additionally, the analysis considers the Navarro–Frenk–White profile (Navarro et al. 1997) dimen-
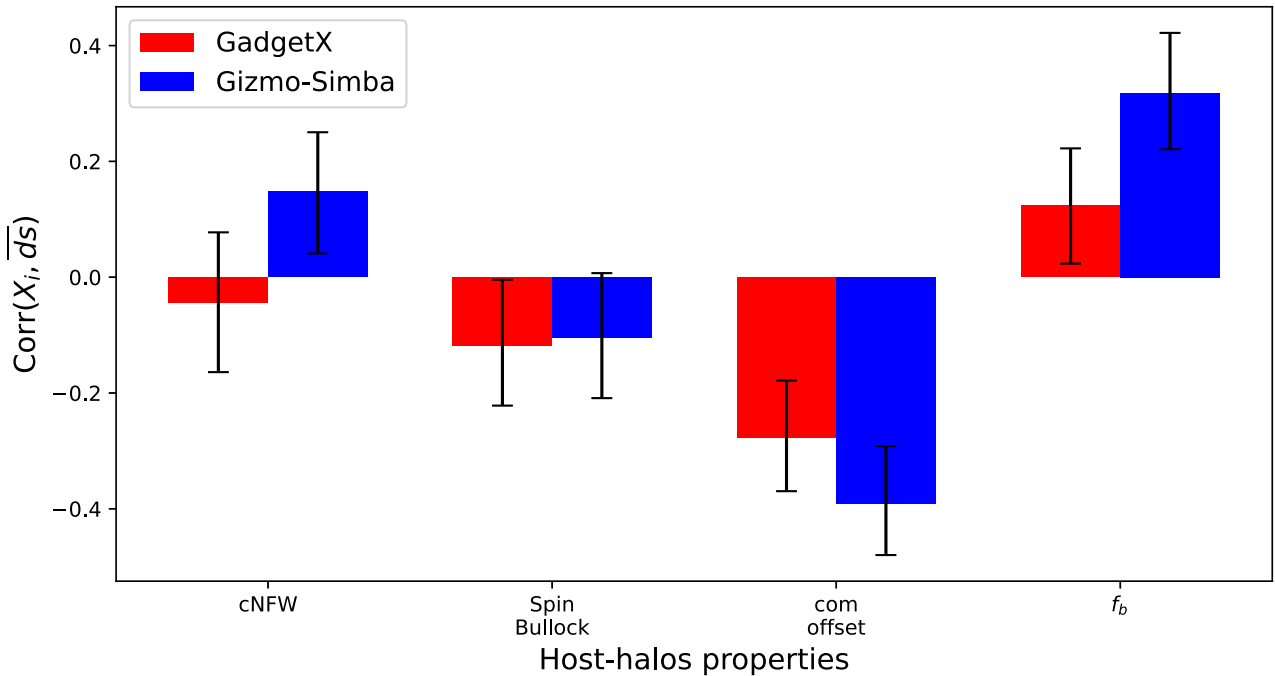
Figure 7. Similar to Fig. 5, but for the correlation between the cluster properties and global residuals ($\overline{ds}$). This correlation can be used to infer the impact of cluster/host-halo physical properties on the $M_{sub}-V_{circ}$ relationship. Once again, we selected sub-haloes from the host clusters that met the following criteria: their mass, $M_{sub} > 1.87 \times 10^{11}$ $M_{\odot}$, and their 2D projected distance, $R_{2D} < 0.15 R_{200c}$. The Spearman correlation coefficients for each host-halo property are accompanied by their respective upper 84 per cent and lower 16 per cent uncertainties.

sionless concentration parameter (cNFW), which characterizes the concentration of the sub-halo's density profile. The concentration parameter, denoted as cNFW, is typically determined by fitting a Navarro–Frenk–White profile to the halo density. It describes how the density of the halo changes with the radial distance from its centre. Here, we simply use the concentration parameter in AHF calculated by following the approach of Prada et al. (2012). They utilize the circular velocity (V_{circ}) and the circular velocity at the virial radius, which is defined in terms of the halo's virial mass and radii. All the other halo properties are introduced in the previous section.

Besides the cNFW parameter, the two simulations show similar correlations with the $\overline{ds}$. GADGET-X suggests that concentrated haloes tend to give a lower $M_{sub}-V_{circ}$ relation, while GIZMO-SIMBA suggests the opposite. However, neither shows a strong relationship with $\overline{ds}$. Both Bullock and Peebles (not shown in the figure) defined spin parameters negatively correlate with $\overline{ds}$, indicating that slow-rotating haloes tend to be closer to the observed fitting line. We report the more robust Bullock spin parameter in Fig. 7. Again, the correlation is not very strong. The highest coefficient is the COM, which suggests that the relaxed haloes tend to agree with observation better. This can be understood as follows: relaxed clusters tend to form earlier (see, e.g. Mostoghiu et al. 2019, for relations between cluster dynamical state, halo formation time, and concentration). Sub-haloes within these clusters have a longer time for stripping, resulting in only the core regions remaining, which, in turn, have a shorter half-mass radius and higher V_{circ}. However, it is worth noting that one cluster, MACSJ0416, in M20, seems to be unrelaxed. This seems contract to our previous prediction. However, we argue that the majority of the sample in M20 (see also Meneghetti et al. (2022)) also are more relaxed. While the simulation sample is more balanced, see De Luca et al. (2021); Zhang et al. (2022).

The positive correlation between $\overline{ds}$ and the halo baryon fraction is in agreement with the correlation result for sub-haloes. It is expected that the higher halo baryon fraction connects with a higher sub-halo baryon fraction. However, it is unclear which is the determined reason: the baryon-rich halo merged into the host halo to bring more baryons or the host halo is baryon rich with the sub-haloes can retain their baryon longer. It is natural to think that a higher halo baryon fraction would induce stronger ram pressure with potentially stronger tidal forces, thus leading to a lower baryon fraction in the sub-haloes. It has been known that the gas in the infalling haloes is easily stripped out (e.g. Haggar et al. 2020b), even before reaching the virial radius of the cluster, this can also happen to the infalling groups as well (see Haggar et al. 2023, for example). Therefore, the baryon fraction for the satellite galaxies is dominated by stars. As it is already shown, the galaxy is more concentrated compared to dark matter, thus less easy to get tidal stripped (see also Contreras-Santos et al. 2024, which is in review). Therefore, it is easy to understand the positive correlation between $\overline{ds}$ and baryon fraction: tidal stripping first removes outlier dark matter particles to result in both high baryon fraction and low sub-halo mass, but the maximum V_{circ} is almost unchanged, as such these sub-haloes tend to be closer to the observation line.

6 CONCLUSIONS

The study by M20 examined the gravitational lensing properties of galaxy clusters and their sub-haloes, revealing a significant discrepancy between observed clusters and hydrodynamic simulations within the ΛCDM cosmology. Notably, observed clusters exhibited a much higher probability of GGSL than simulated clusters. Moreover, they utilized maximum circular velocities (V_{circ}) of sub-haloes as a metric to assess compactness, finding that sub-haloes in observed clusters had higher V_{circ} values compared to those in mass-matched

clusters from simulations. This suggests that galaxies in observed clusters are more efficient at lensing background sources and are more compact than those in the simulations. In this study, we thoroughly investigated the discrepancy between the simulations and observations discussed in M20.

In our study, we used simulated clusters from the THE THREE HUNDRED project Cui et al. (2018, 2022) with masses $M_{200} > 9.59 \times 10^{14}$ M$_\odot$. We aimed to compare these simulated clusters with the observations of three primary reference clusters of M20 that have a median redshift of $z = 0.39$. We selected a sample of 90 host clusters from GADGET-X simulation and 82 host clusters from GIZMO-SIMBA simulation at a redshift of $z = 0.394$ to compare it fairly with observations of M20. We then expanded our analysis by including host clusters at two additional redshifts: $z = 0.194$ and $z = 0$ for evolutionary studies. The selected clusters at $z = 0.194$ for GADGET-X and GIZMO-SIMBA are 180 and 169, respectively. Similarly, at redshift $z = 0$, GADGET-X and GIZMO-SIMBA provide 321 and 302 cluster samples. Further details about our sample of selected clusters and their sub-haloes can be found in Table 1 and Table 2. In our analysis, we found the following:

(i) The cumulative sub-halo mass function shows an overall consistency between MACSJ0416 and MACSJ1206 clusters from M20 and the GIZMO-SIMBA simulation with $R_{2D} < 0.15R_{200c}$ (Fig. 1, left). However, for GADGET-X, agreement between the observation and simulation is only found at a higher sub-halo mass range. The discrepancy at the low-mass end is attributed to a stronger resolution dependence in the baryon model of GADGET-X. The 2D versus 3D comparison of the sub-halo mass function (as shown in Fig. 1) highlights the substantial impact of projection effects, revealing a two-fold increase in sub-halo numbers in 2D compared to 3D.

(ii) The redshift evolution study of cumulative sub-halo mass function reveals that while the median halo mass increases with decreasing redshift, the number of sub-haloes within massive clusters decreases toward the present time. The analysis of the normalized sub-halo mass function shows a clear redshift evolution, where a greater number of sub-haloes are expected to be observed at earlier times when they are less concentrated within their host haloes. The sub-halo mass function for both GADGET-X and GIZMO-SIMBA at $z = 0$ is lower (fewer sub-haloes) compared to $z = 0.394$, indicating a decrease in the number of sub-haloes within host haloes over time (as shown in Fig. 2).

(iii) Both GADGET-X and GIZMO-SIMBA simulations consistently show lower circular V_{circ} for sub-haloes compared to the fitting line obtained from observations when following the distance constraint $R_{2D} < 0.15R_{200c}$. However, GIZMO-SIMBA exhibits slightly higher V_{circ} values than GADGET-X. Furthermore, GIZMO-SIMBA shows a weak redshift evolution with higher V_{circ} at $z = 0.394$ compared to $z = 0$, unlike GADGET-X.

(iv) The M_{sub}–V_{circ} relationship for sub-haloes with masses $M_{sub} < 1.47 \times 10^{11}$ M$_\odot$ still shows a noticeable difference between observations and simulations. As shown in Fig. 4, this redshift evolution can not account for the discrepancy between the observed and simulated results. This discrepancy is particularly relevant in the context of GGSL. Alternatively, when considering massive sub-haloes with $M_{sub} > 5.90 \times 10^{11}$ M$_\odot$, where simulations are a bit closer to the observed fitting relation – albeit not in perfect agreement–the significance of the discrepancy decreases due to the limited number of observed sub-haloes within this mass range. However, it's important to note that, in this range of sub-halo masses, the observed fitting relation of M20 is extrapolated. While different results obtained from GADGET-X and GIZMO-SIMBA simulations suggest a potential

solution to this problem through fine tuning the baryon models used in the simulations, it is not guaranteed, as results from GIZMO-SIMBA are still not compatible with the observation result, albeit somewhat closer than GADGET-X. Furthermore, we refer to Meneghetti et al. (2023) for a similar conclusion on the GGSL signal.

(v) The Spearman correlation analysis between sub-halo/galaxy properties and the residual ds reveals that both simulations agree that there is a correlation or anticorrelation between ds and various sub-halo/galaxy properties, see Fig. 5. The significant sub-halo properties that notably impact the residual ds are the galaxy stellar age, distance from the cluster's centre (R_{3D}), sub-halo half mass radius, and baryon fraction. The Spearman correlation value indicates that the half-mass radius of the sub-halo and being further away from the centre of the cluster are associated with a more significant deviation from the observed M_{sub}–V_{circ} relation. Alternatively, older galaxy stellar age (formed earlier) and higher sub-halo baryonic mass fraction tend to bring the simulated sub-halo V_{circ} closer to the observed relation.

(vi) Upon comparing the sub-halo properties of GADGET-X and GIZMO-SIMBA, it is evident that GADGET-X exhibits slightly higher baryonic content in its simulated clusters' sub-haloes (Fig. 6). Additionally, the distribution of galaxy ages is highly comparable between GADGET-X and GIZMO-SIMBA, with a slightly higher proportion of young galaxies in GADGET-X (Fig. 6). Specifically, the size and concentration of sub-haloes/galaxies are identified as crucial factors that contribute to the differences in the M_{sub}–V_{circ} relation, with GIZMO-SIMBA having smaller sizes and higher concentrations compared to GADGET-X. The differences in sub-halo properties imply that creating even more compact sub-haloes/galaxies, maybe through an even earlier galaxy formation, may result in an improved model-observational data alignment.

(vii) Investigation of global host halo properties in relation to the M_{sub}–V_{circ} relationship reveals that relaxed haloes exhibit the strongest alignment with observations (negative correlation with COM offset and $\overline{ds}$). A modest negative correlation between spin parameters and $\overline{ds}$ indicates a tendency for slow-rotating haloes to be closer to the observed fitting line, albeit with a weak correlation. Additionally, a positive correlation is observed between $\overline{ds}$ and the halo baryon fraction, suggesting a connection to the baryon fraction of sub-haloes Fig. 7.

In conclusion, our analysis of galaxy clusters simulated using both GADGET-X and GIZMO-SIMBA in the THE THREE HUNDRED project reveals a discrepancy when comparing them to observations of M20. Our findings suggest that our contemporary simulations still struggle to faithfully replicate the observed compactness of sub-haloes, thus the M_{sub}–V_{circ} relation. This disparity may arise from limitations in many aspects, such as baryonic modelling, systematic challenges within our simulation approaches, and uncertainties in observational data and their modelling. In addition, it is also necessary to note here that the comparison done in this paper is based on the AHF halo catalogue instead of SUBFIND in previous studies. We refer to Onions et al. (2012) and Castro et al. (2023) for detailed comparisons between different sub-halo finders and discussions. Both AHF and SUBFIND have unbinding processes to remove the particles that are not gravitationally bound to the sub-halo. This is inconsistent with the sub-halo mass measured in observation which suffers from the projection effect. Apart from that, using the observed sub-halo mass through the lensing technique may also increase the discrepancy between the simulated and observed relations. Lastly, our simulation is based on the ΛCDM framework. Consequently, we cannot explore the impact of alternative frameworks, such as warm dark matter and alternative dark energy models, on the M_{sub}–V_{circ} relation.

7 DATA AVAILABILITY

The data underlying this article will be shared on reasonable request to the corresponding author. The simulation data are provided by the 300 collaboration which can also be accessed upon request on their website.

REFERENCES

Anglés-Alcázar D., Özel F., Davé R., Katz N., Kollmeier J. A., Oppenheimer B. D., 2015, ApJ, 800, L127
Anglés-Alcázar D., Davé R., Faucher-Giguère C.-A., Özel F., Hopkins P. F., 2017a, MNRAS, 464, 2840
Anglés-Alcázar D., Faucher-Giguère C.-A., Kereš D., Hopkins P. F., Quataert E., Murray N., 2017b, MNRAS, 470, 4698
Ansarifard S. et al., 2020, A&A, 634, 113
Armitage T. J., Kay S. T., Barnes D. J., Bahé Y. M., Dalla Vecchia C., 2019, MNRAS, 482, 3308
Arthur J. et al., 2019, MNRAS, 484, 3968
Bahé Y. M., 2021, MNRAS, 505, 1458
Bahé Y. M. et al., 2019, MNRAS, 485, 2287
Beck A. M. et al., 2016, MNRAS, 455, 2110
Bergamini P. et al., 2019, A&A, 631, 130
Bhattacharyya S., Adhikari S., Banerjee A., More S., Kumar A., Nadler E. O., Chatterjee S., 2022, ApJ, 932, L30
Bondi H., 1952, MNRAS, 112, 195
van den Bosch F. C., Ogiya G., Hahn O., Burkert A., 2018, MNRAS, 474, 3043
Bullock J. S., Kolatt T. S., Sigad Y., Somerville R. S., Kravtsov A. V., Klypin A. A., Primack J. R., Dekel A., 2001, MNRAS, 321, 559
Castro T. et al., 2023, A&A, 671, 100
Chabrier G., 2003, PASP, 115, 763
Choi E., Ostriker J. P., Naab T., Johansson P. H., 2012, ApJ, 754, L125
Contreras-Santos A., Knebe A., Cui W., Haggar R., Pearce F., Gray M., De Petris M., Yepes G., 2023, MNRAS, 522, 1270
Cui W., 2022, EPJ Web Conf. Volume 257, mm Universe @ NIKA2 - Observing the mm Universe with the NIKA2 camera, EPJ Web Conf., 00011. Available at: https://doi.org/10.1051/epjconf/202225700011
Cui W., Power C., Borgani S., Knebe A., Lewis G. F., Murante G., Poole G. B., 2017, MNRAS, 464, 2502
Cui W. et al., 2018, MNRAS, 480, 2898
Cui W. et al., 2022, MNRAS, 514, 977
Davé R., Thompson R., Hopkins P. F., 2016, MNRAS, 462, 3265
Davé R., Anglés-Alcázar D., Narayanan D., Li Q., Rafieferantsoa M. H., Appleby S., 2019, MNRAS, 486, 2827
de Andres D. et al., 2022, Nature Astron., 6, 1325
De Luca F., De Petris M., Yepes G., Cui W., Knebe A., Rasia E., 2021, MNRAS, 504, 5383
Despali G., Lovell M., Vegetti S., Crain R. A., Oppenheimer B. D., 2020, MNRAS, 491, 1295
Diemer B., More S., Kravtsov A. V., 2013, ApJ, 766, L25
Ferragamo A. et al., 2023, MNRAS, 520, 4000
Finkelstein S. L. et al., 2022, ApJ, 940, L55
Gao L., White S. D., Jenkins A., Stoehr F., Springel V., 2004, MNRAS, 355, 819
Gao L., Frenk C., Boylan-Kolchin M., Jenkins A., Springel V., White S., 2011, MNRAS, 410, 2309
Giocoli C., Moreno J., Sheth R. K., Tormen G., 2007, MNRAS, 376, 977
Giocoli C., Tormen G., Van Den Bosch F. C., 2008, MNRAS, 386, 2135
Giocoli C., Tormen G., Sheth R. K., van den Bosch F. C., 2010, MNRAS, 404, 502
Green S. B., van den Bosch F. C., Jiang F., 2021, MNRAS, 503, 4075
Haardt F., Madau P., 1996, ApJ, 461, 20
Haardt F., Madau P., 2012, ApJ, 746, L125
Haggar R., Gray M. E., Pearce F. R., Knebe A., Cui W., Mostoghiu R., Yepes G., 2020b, MNRAS, 492, 6074
Haggar R., Gray M. E., Pearce F. R., Knebe A., Cui W., Mostoghiu R., Yepes G., 2020a, MNRAS, 492, 6074
Haggar R., Kuchner U., Gray M. E., Pearce F. R., Knebe A., Yepes G., Cui W., 2023, MNRAS, 518, 1316
Hopkins P. F., 2015, MNRAS, 450, 53
Joshi G. D., Parker L. C., Wadsley J., Keller B. W., 2019, MNRAS, 483, 235
Klypin A., Yepes G., Gottlöber S., Prada F., Hess S., 2016, MNRAS, 457, 4340
Knollmann S. R., Knebe A., 2009, ApJS, 182, 608
Kuchner U. et al., 2020, MNRAS, 494, 5473
Li Q. et al., 2020, MNRAS, 495, 2930
Li Q. et al., 2023, MNRAS, 523, 1228
Lotz J. M. et al., 2017, ApJ, 837, L97
Meneghetti M. et al., 2020, Science, 369, 1347
Meneghetti M. et al., 2022, A&A, 668, 188
Meneghetti M. et al., 2023, A&A, 678, L2
Mostoghiu R., Knebe A., Cui W., Pearce F. R., Yepes G., Power C., Dave R., Arth A., 2019, MNRAS, 483, 3390
Murante G., Monaco P., Giovalli M., Borgani S., Diaferio A., 2010, MNRAS, 405, 1491
Naidu R. P. et al., 2022, ApJ, 940, L14
Navarro J. F., Frenk C. S., White S. D. M., 1997, ApJ, 490, 493
Nelson D. et al., 2019, Computational Astrophysics and Cosmology, 6, 1
Onions J. et al., 2012, MNRAS, 423, 1200
Peebles P., 1969, ApJ, 155, L393
Pillepich A. et al., 2018, MNRAS, 475, 648
Planck Collaboration et al., 2016, A&A, 594, 13
Planelles S., Borgani S., Fabjan D., Killedar M., Murante G., Granato G. L., Ragone-Figueroa C., Dolag K., 2014, MNRAS, 438, 195
Planelles S. et al., 2017, MNRAS, 467, 3827
Postman M. et al., 2012, ApJS, 199, 25
Power C., Navarro J. F., Jenkins A., Frenk C. S., White S. D., Springel V., Stadel J., Quinn T., 2003, MNRAS, 338, 14
Prada F., Klypin A. A., Cuesta A. J., Betancort-Rijo J. E., Primack J., 2012, MNRAS, 423, 3018
Ragagnin A. et al., 2022, A&A, 665, 16
Ragone-Figueroa C., Granato G. L., Ferraro M. E., Murante G., Biffi V., Borgani S., Planelles S., Rasia E., 2018, MNRAS, 479, 1125
Rahmati A., Pawlik A. H., Raičevic M., Schaye J., 2013, MNRAS, 430, 2427
Rasia E. et al., 2015, ApJ, 813, L17
Robertson A., 2021, MNRASL, 504, 7
Rost A. et al., 2021, MNRAS, 502, 714

Sayers J., Mantz A. B., Rasia E., Allen S. W., Cui W., Golwala S. R., Morris R. G., Wan J. T., 2023, ApJ, 944, L221

Sembolini F., Yepes G., De Petris M., Gottlöber S., Lamagna L., Comis B., 2013, MNRAS, 429, 323

Sereno M., Lovisari L., Cui W., Schellenberger G., 2021, MNRAS, 507, 5214

Smith B. D. et al., 2017, MNRAS, 466, 2217

Springel V., 2005, MNRAS, 364, 1105

Springel V., Hernquist L., 2003, MNRAS, 339, 289

Springel V., White S. D., Tormen G., Kauffmann G., 2001, MNRAS, 328, 726

Springel V. et al., 2018, MNRAS, 475, 676

Steinborn L. K., Dolag K., Hirschmann M., Prieto M. A., Remus R.-S., 2015, MNRAS, 448, 1504

Tormen G., 1998, MNRAS, 297, 648

Tornatore L., Borgani S., Dolag K., Matteucci F., 2007, MNRAS, 382, 1050

White S. D., Frenk C. S., 1991, ApJ, 379, L52

Wiersma R. P., Schaye J., Smith B. D., 2009, MNRAS, 393, 99

Yang D., Yu H.-B., 2021, Phys. Rev. D, 104, 103031

Zhang B., Cui W., Wang Y., Dave R., De Petris M., 2022, MNRAS, 516, 26

APPENDIX A: CONVERGENCE TEST ON THE SUB-HALO MASS FUNCTION

We conducted a simple analysis to assess the convergence of the sub-halo mass functions between the two simulation models, namely GADGET-X and GIZMO-SIMBA. The sub-halo mass functions of the low-resolution GIZMO-SIMBA simulation runs (the default set of THE THREE HUNDRED simulations) are then also compared with the high-resolution (8 times more particles) GIZMO-SIMBA simulation runs. For this test, we focused on the sub-halo samples within the modelled clusters at redshift $z = 0$. The sub-halo mass function for one of the modelled cluster regions, chosen from the total of 324 simulated cluster regions in the THE THREE HUNDRED project, is shown in Fig. A1. No sub-halo mass constraints, stellar mass constraints, or radial cutoffs were applied to these sub-halo samples. We used all the sub-haloes within the halo virial radius R_{200c} to test the convergence of the sub-halo mass function.

Fig. A1 depicts the sub-halo mass functions for the low-resolution GADGET-X (red-dashed dot) and GIZMO-SIMBA (green-dotted line) simulations, along with the high-resolution GIZMO-SIMBA run (blue), all plotted together. We can infer from the plot that the sub-halo mass function converges down to $\sim 3 \times 10^{10}\,\mathrm{M_\odot}$ between the high- and low-resolution GIZMO-SIMBA runs. However, the deviation between GADGET-X and GIZMO-SIMBA starts at a little bit higher mass, $\sim 1.27 \times 10^{11}\,\mathrm{M_\odot}$. Therefore, the vertical dotted line which marks the mass cut in this paper, works well for selecting the convergence sub-halo samples. The flattened curve of GADGET-X at the lower sub-halo mass range could be due to the strong SN feedback as discussed in Section 3 of the main article.
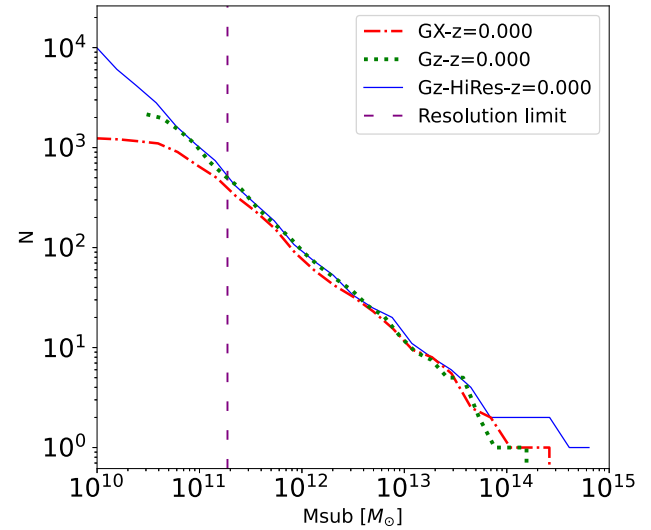

Figure A1. Comparisons between the cumulative sub-halo mass function for sub-haloes within one of the modelled clusters of the THE THREE HUNDRED project, simulated using both GADGET-X and GIZMO-SIMBA baryon models. The red dashed dot and green dotted line correspond to the sub-halo mass functions for the low-resolution version of the simulation discussed in this manuscript, representing the GADGET-X and GIZMO-SIMBA runs, respectively. The blue solid line represents the sub-halo mass function from the high-resolution GIZMO-SIMBA run. The dashed vertical line in purple corresponds to sub-halo mass threshold of $M_{\mathrm{sub}} = 1.87 \times 10^{11}\,\mathrm{M_\odot}$, which also indicates the resolution limit.

This paper has been typeset from a TeX/LaTeX file prepared by the author.